THE ASTROPHYSICAL JOURNAL, 521:889–897, 1999 August 20

QUASI-SEPARATRIX LAYERS IN A REDUCED MAGNETOHYDRODYNAMIC MODEL OF A CORONAL LOOP

LEONARDO J. MILANO,[1] PABLO DMITRUK,[2] CRISTINA H. MANDRINI,[3] AND DANIEL O. GÓMEZ[3]
Instituto de Astronomía y Física del Espacio, CC. 67 Suc. 28, 1428 Buenos Aires, Argentina; and Departamento de Física, Facultad de Ciencias Exactas y Naturales, Universidad de Buenos Aires, C. Universitaria, 1428 Buenos Aires, Argentina; leo@iafe.uba.ar

AND

PASCAL DÉMOULIN
Observatoire de Paris, section Meudon, DASOP, URA 2080 (CNRS), F-92195 Meudon Principal Cedex, France
Received 1998 August 21; accepted 1999 April 2

ABSTRACT

We run a pseudospectral magnetohydrodynamic code to simulate reconnection between two flux tubes inside a solar coronal loop. We apply a stationary velocity field at one of the footpoints consisting of two vortices in such a way as to induce the development of a current layer and force the field lines to reconnect. During the process we find a remarkable coincidence between the location of the current layer and the location of quasi-separatrix layers, which are thin magnetic volumes where the field line connectivity changes abruptly. This result lends support to a scenario in which quasi-separatrix layers are the most likely locations for impulsive energy release in the solar corona. Another important result of this simulation is the observed transient of strong magnetohydrodynamic turbulence characterized by a $k^{-3/2}$ energy spectrum. This transient reaches its peak activity in coincidence with a maximum in the energy dissipation rate, thus suggesting that the direct energy cascade associated with this turbulent transient plays a key role in enhancing energy dissipation in magnetic reconnection processes.
Subject headings: MHD — Sun: corona — Sun: flares — Sun: magnetic fields

1. INTRODUCTION

Solar coronal loops are driven at their footpoints by the photospheric velocity field. Although the typical timescale for this driving action is relatively slow (about 1000 s), it can give rise to reconnection phenomena occurring on the much shorter Alfvén time (10–100 s). These impulsive reconnection events involve changes in the magnetic topology and the formation of current sheets where the magnetic energy is efficiently dissipated.

The basic picture of externally driven reconnection is that of two flux tubes pushed into one another along with the fluid in a quasi-ideal flow until they come close enough so that the electric current density in between, $\boldsymbol{j} = \nabla \times \boldsymbol{B}$, grows up dramatically, yielding to nonnegligible local Joule dissipation (ηj^2). Local loss of ideal conditions allows a relative drift of magnetic field lines with respect to the fluid. As a result, after a short time (of the order of the local Alfvén time) the magnetic tubes appear reconnected, that is, literally connected in a new way, which is topologically different from the initial configuration (see, e.g., Longcope & Strauss 1994a).

In two dimensions the magnetic topology is fully determined by the scalar magnetic potential a (where $\boldsymbol{B} = \nabla \times a\hat{z}$). In this approach, magnetic reconnection is associated with the presence of magnetic null points (X-points or Y-points) or field lines tangential to a boundary. Reconnection occurs at separatrices, which are lines where the magnetic field line mapping is discontinuous. Although the same analysis is possible in 2.5 dimensions, it has been shown that the addition of three-dimensional perturbations (Lau & Finn 1991) typically causes the disappearance of separatrices (Longcope & Strauss 1994b). The existence of this structural instability has lead to the investigation of different approaches to extend the topological ideas introduced in two-dimensional models, but no consensus has yet been reached for a proper definition of reconnection (see, e.g., Jardine 1991; Priest 1997).

A promising way of quantifying topological changes has been proposed in terms of quasi-separatrix layers (QSLs) (Priest & Démoulin 1995; Démoulin et al. 1996a). QSLs are extremely thin layers where the gradient of the mapping of field lines from one portion to another of a boundary enclosing a magnetic volume is much larger than its standard value (by several orders of magnitude). Reconnection without null points can then occur at QSLs, where there is a breakdown of ideal magnetohydrodynamics (MHD) and a change of connectivity of magnetic field lines. Priest & Démoulin (1995) have proposed that this change of connectivity occurs where the field line velocities are much larger than the maximum plasma velocity (typically less than or of the order of the Alfvén speed), so that the field lines are forced to slip through the plasma.

Analysis of solar flare observations in numerous cases has shown that the release of energy is linked to the presence of separatrices or QSLs (see Mandrini et al. 1997 and references therein). In these cases the photospheric magnetic field is extrapolated to the corona by means of either subphotospheric sources or following a classical fast Fourier transform method (Alissandrakis 1981). On the other hand, QSLs have been found to be related to expected energy release sites in theoretical models of twisted flux tubes (Démoulin et al. 1996b) and in application of these to observed filaments (Aulanier et al. 1998). In this paper we compute for the first time QSLs for an MHD model of a coronal loop and study the relation between the location of QSLs and the region of high-energy dissipation inside this

[1] Fellow of CONICET, Argentina.
[2] Fellow of the University of Buenos Aires.
[3] Member of the Carrera del Investigador Científico, CONICET, Argentina.

loop. In §§ 2 and 3 we describe the numerical simulations that we perform, with a brief presentation of the basic equations and of the applied photospheric forcing. A description of the results obtained from those simulations within the frame of reconnection theory is presented in § 4. A definition of QSLs and a comparison with the results derived from our simulations is presented in § 5. In § 6 we discuss our results and list the conclusions of this paper.

2. EQUATIONS FOR REDUCED MAGNETOHYDRODYNAMICS

The dynamics of a coronal loop with an initially uniform magnetic field $\boldsymbol{B} = B_0 \hat{z}$, length L, and transverse section $(2\pi l) \times (2\pi l)$ can be modeled by the reduced magnetohydrodynamic (RMHD) equations (see Strauss 1976 for a detailed derivation of these equations),

$$\partial_t a = v_A \partial_z \psi + [\psi, a] + \eta \nabla_\perp^2 a , \qquad (1)$$

$$\partial_t w = v_A \partial_z j + [\psi, w] - [a, j] + \nu \nabla_\perp^2 w . \qquad (2)$$

In these equations, $v_A = B_0/(4\pi\rho)^{1/2}$ is the Alfvén speed, ν is the kinematic viscosity, η is the plasma resistivity, $\psi(x, y, z, t)$ is the stream function, and $a(x, y, z, t)$ is the vector potential. The quantities $w = -\nabla_\perp^2 \psi$ and $j = -\nabla_\perp^2 a$ are, respectively, the z-component of vorticity and electric current density, where $\nabla_\perp^2 = \partial_{xx} + \partial_{yy}$. The nonlinear terms are Poisson brackets of the form $[u, v] = \partial_x u \partial_y v - \partial_y u \partial_x v$. Transverse velocity and magnetic field components are given by $\boldsymbol{v} = \nabla \times (\psi \hat{z})$ and $\boldsymbol{b} = \nabla \times (a\hat{z})$.

3. NUMERICAL SIMULATIONS

To transform equations (1) and (2) into their dimensionless form, we choose l and L as the units for transverse and longitudinal distances, $t_A \equiv L/v_A$ as the time unit, and $u_0 \equiv l/t_A$ as the unit for the velocity and magnetic fields. The dimensionless RMHD equations are

$$\partial_t a = \partial_z \psi + [\psi, a] + \frac{1}{S} \nabla_\perp^2 a , \qquad (3)$$

$$\partial_t w = \partial_z j + [\psi, w] - [a, j] + \frac{1}{R} \nabla_\perp^2 w , \qquad (4)$$

where $S = u_0 l/\eta$ and $R = u_0 l/\nu$. For our simulations, R and S are, respectively, good estimates of the kinetic ($\langle u^2 \rangle^{1/2} l/\nu$) and magnetic ($\langle u^2 \rangle^{1/2} l/\eta$) Reynolds numbers. Hereafter, we thus call R and S, respectively, the kinetic and magnetic Reynolds numbers. The spatial coordinates span the ranges $0 \leq x, y \leq 2\pi$ and $0 \leq z \leq 1$.

We performed numerical simulations of equations (3) and (4) assuming periodic boundary conditions for both ψ and a in the x- and y-directions and given stream functions in the $z = 0$ and $z = 1$ planes, which represent the forcing of the photospheric velocity field over the loop footpoints. The magnetic vector potential and the stream function are expanded in Fourier modes in each plane (x, y). The equations for the coefficients $\psi_{\boldsymbol{k}}(z, t)$ and $a_{\boldsymbol{k}}(z, t)$ are time evolved using a second-order predictor-corrector scheme, and the nonlinear terms are evaluated following a $\frac{2}{3}$ dealiased (see Canuto et al. 1988) pseudospectral technique (see also Dmitruk, Gómez, & DeLuca 1998)

To compute z-derivatives we use a Chebyshev collocation method, instead of the standard method of finite differences in a staggered regular grid (see, for instance, Strauss 1976). Gauss-Lobatto collocation points are used, which are mostly concentrated near the boundaries. The main advantage of this collocation technique is that we reach 99% accuracy with approximately half of the grid points required with a regularly spaced mesh. To test the accuracy of our simulations, we check the balance of energy E and cross helicity H per unit loop length:

$$\partial_t E = v_A \partial_z H - \int (\eta j^2 + \nu w^2) d^2x , \qquad (5)$$

$$\partial_t H = v_A \partial_z E - (\eta + \nu) \int \boldsymbol{w} \cdot \boldsymbol{j}\, d^2x , \qquad (6)$$

where

$$E(z, t) = \tfrac{1}{2} \int (u^2 + b^2) d^2x , \qquad (7)$$

$$H(z, t) = \int \boldsymbol{u} \cdot \boldsymbol{b}\, d^2x . \qquad (8)$$

Equations (5) and (6) are readily obtained from equations (1) and (2) for the case of periodic boundary conditions, both for an infinite or a truncated Fourier expansion. Note that $E(z, t)$ in equation (7) corresponds to the free energy per unit length of the loop. The total energy is obtained by adding to the right-hand side of equation (7) the contribution of the main field, $v_A^2/2(2\pi l)^2$. Since this last contribution is a constant in RMHD (which is not available for dissipation), we will disregard it and call $E(z, t)$ the energy of the loop.

A set of numerical runs with the same boundary and initial conditions but different Reynolds numbers was performed. As a boundary condition at the $z = 1$ and $z = 0$ planes (photospheric footpoints) we choose a stream function of the form

$$\psi(x, y, 1, t) = \Phi_0 \left\{ \exp\left[-\frac{(x - x_1)^2 + (y - y_1)^2}{d^2} \right] + \exp\left[-\frac{(x - x_2)^2 + (y - y_2)^2}{d^2} \right] \right\} \equiv \Phi(x, y) ,$$

$$\psi(x, y, 0, t) = 0 , \qquad (9)$$

where $x_{1,2} = \pm\pi/4 = y_{1,2}$ and $d = 2\pi/7$. The stream function Φ represents two parallel vortices of equal intensity centered at (x_1, y_1) and (x_2, y_2), as shown in Figure 1. The initial condition is

$$\psi(x, y, z, 0) = z\Phi(x, y) , \quad a(x, y, z, 0) = 0 , \qquad (10)$$

that is, no transverse magnetic field and a linear interpolation of the velocity field between its values at $z = 0$ and $z = 1$.

The strength of the forcing is given by the photospheric velocity u_{ph}, which corresponds to the rms value of the velocity field applied at the moving boundary ($z = 1$). The normalization factor Φ_0 in equation (9) is thus proportional to t_A/t_{ph}, where $t_{ph} \equiv l/u_{ph}$ is the photospheric turnover time. Another dimensionless parameter, which is relevant to a topological analysis of magnetic field lines (see § 5) is the aspect ratio $2\pi l/L$. Note that our footpoint motions are given by a stationary and nonrandom velocity field. In this regard it is different from other simulations of coronal loop dynamics, such as those performed by Galsgaard & Nordlund (1996), Mikic, Schnack, & van Hoven (1989), or van

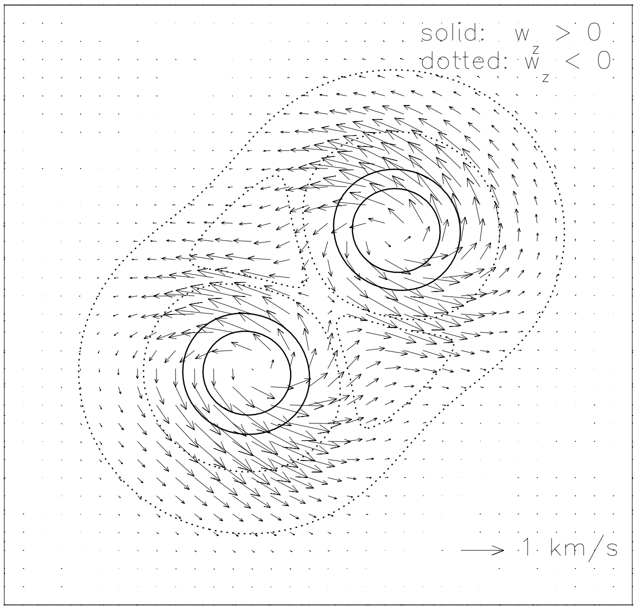

FIG. 1.—Vorticity contours and velocity field at $z = 1$ (photospheric boundary condition for the loop).

Ballegooijen (1986), where random footpoint motions are applied.

We choose for our simulations $t_A/t_{ph} = 0.016$, $2\pi l/L = 0.1$, and various Reynolds numbers in the range $100 \le R, S \le 700$. However, all the results we report correspond to our $S = R = 500$ case, unless otherwise stated. The number of grid points is $96 \times 96 \times 16$. For simplicity, we set the Prandtl number to unity ($\mathrm{Pr} = \nu/\eta = 1$, i.e., $R = S$) in all simulations. As typical photospheric quantities, we choose $l = 10^3$ km and $u_{ph} = 1$ km s^{-1}. Assuming a coronal density of 10^{10} cm^{-3}, the vertical magnetic field turns out to be $B_z = 90$ G.

4. RESULTS

Starting from the initial condition described in equation (10), we obtain solutions which, at short times ($t < 5t_A$), are very close to the following direct current behavior:

$$\psi(x, y, z, t) = z\Phi(x, y)\ , \quad a(x, y, z, t) = t\Phi(x, y)\ . \quad (11)$$

These expressions are exact solutions to the ideal and linearized RMHD equations. The magnetic field in this early stage grows linearly in time and topologically corresponds to two continuously twisted flux tubes, as shown in Figure 3*a*. Each of these tubes contains a positive kernel of electric current density j.

Energy dissipation is negligible for this rather laminar evolutionary stage. Extrapolation in time of this linear solution leads to a serious departure from the real solution, as shown, for instance, in Figure 2, which shows the energy (Fig. 2*a*) and the energy dissipation rate (Fig. 2*b*) as a function of time. This is not surprising, since nonlinearities and dissipation become more important as time progresses. Notwithstanding, as discussed below (see § 5), the information about the sites of intense energy dissipation (QSLs) is already present in the simple linear solution shown in equation (11).

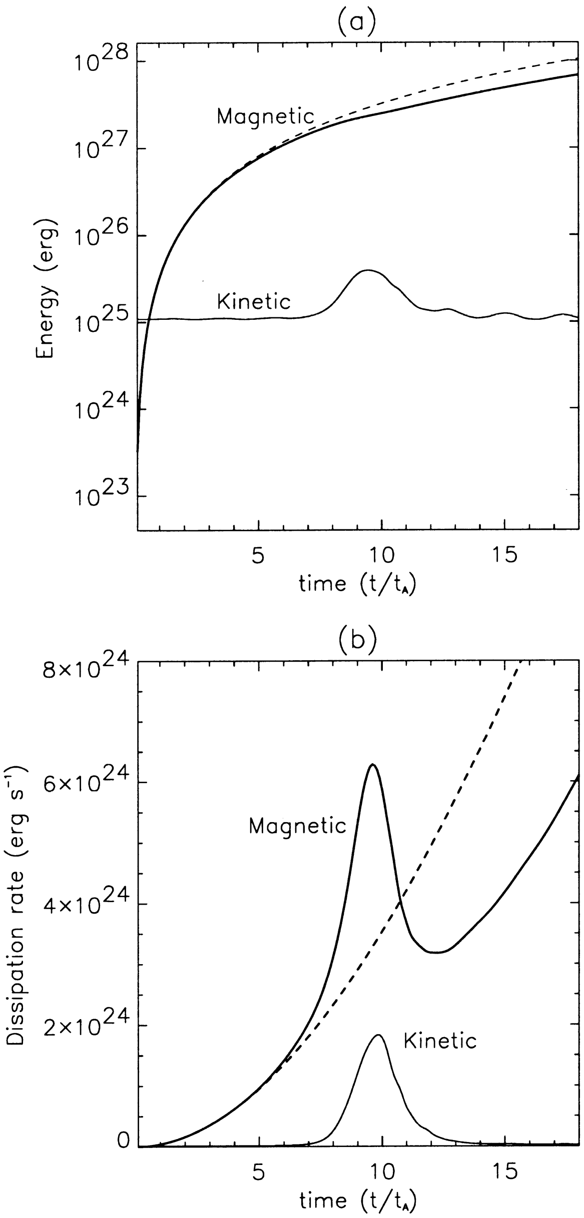

FIG. 2.—Temporal evolution of energy and dissipation. (*a*) Magnetic and kinetic energy as a function of time. The dashed line represents the magnetic energy of the ideal and linear case (eq. [11]). The burst in kinetic energy is due to the Alfvénic outflows during the reconnection process. (*b*) Magnetic and kinetic energy dissipation rate as a function of time. The dashed line corresponds for the linear solution.

During the linear stage the electric current confined in each kernel grows linearly in time. The attractive force between these parallel currents accelerates them to each other leading to magnetic field compression and the development of a current layer, which becomes apparent by $t \approx 9t_A$, when nonlinear effects become dominant. This reconnection process is highly dissipative, as shown in Figure 2. For $t < 5t_A$, magnetic dissipation and energy grow like t^2, as predicted by equation (11) (Figs. 2*a* and 2*b*, *dotted curve*), but for $7t_A < t < 11t_A$ there is a dramatic enhancement in both kinetic and magnetic energy dissipation.

The change in connectivity involved in the reconnection process taking place by $t \approx 9t_A$, and the coalescence of the

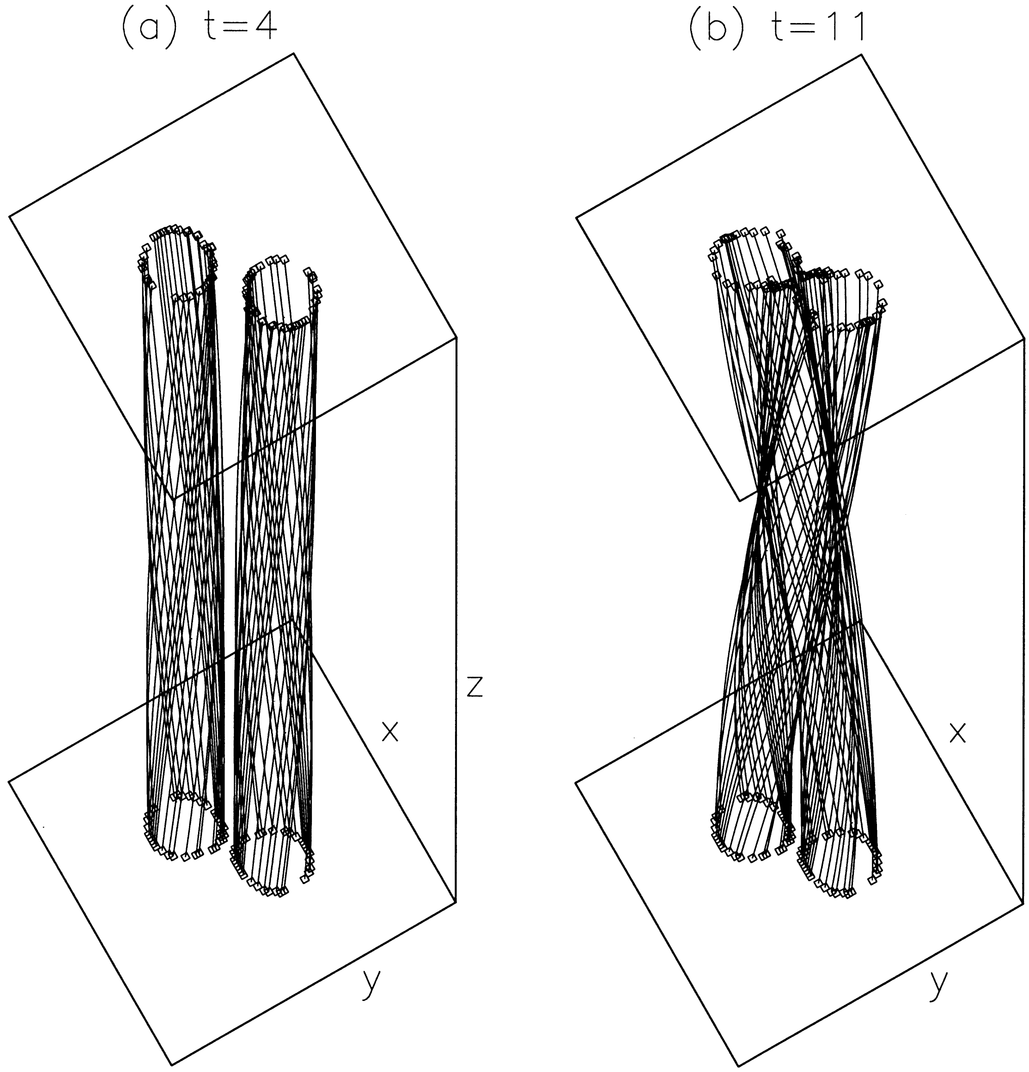

FIG. 3.—Coalescence of two flux tubes. (*a*) Magnetic field lines at $t = 4t_A$. (*b*) Same as *a*, but for $t = 11t_A$. Field lines begin at the same points in the $z = 0$ plane for both figures.

attracting flux tubes, is shown in Figure 3. Figure 3*a* shows several magnetic field lines at $t = 4t_A$, corresponding to two well-separated flux tubes. Most of the magnetic energy of the loop is contained in those tubes. Figure 3*b* shows (at $t = 11t_A$) a set of field lines intersecting the $z = 0$ plane at the same points of the field lines in Figure 3*a*. It is clear that the field lines have dramatically changed their connectivity, giving a global aspect of a single flux tube, as a result of the coalescence of the original tubes. These results are in full agreement with those of Longcope & Strauss (1994a) where they study the development of coalescence in an unstable initial configuration formed by multiple flux tubes of alternating helicity.

Figure 4 displays the spatial distribution of the electric current density and the velocity field at the half-length of the loop ($z = 0.5$). Figure 4*a* shows a classical picture of two-dimensional reconnection. Two kernels of positive current are being pushed together by their attractive force, leading to the formation of an intense (negative) current layer in between. The fluid enters the reconnection layer from both sides and is expelled at the edges at a much greater speed. Figure 4*b* corresponds to the time where the dissipation rate is at its maximum ($t \approx 9.7t_A$). Although the overall picture is quite comparable to the one we just described, the Alfvénic jets and the current layer itself look tilted and skewed with respect to their previous orientation, featuring a less symmetric pattern.

We computed the reconnection rate for the cases $S = R = 400, 500, 600, 700$. As suggested by DeLuca & Craig (1992) for a dynamical reconnection process, we estimated the reconnection rate as $\eta j_{\max}$. Although our Reynolds numbers are rather moderate and do not span a sufficiently wide interval, we find that the process under study is compatible with a fast reconnection scenario, since the reconnection rate scales like a rather small power of the resistivity, i.e., $\eta j_{\max} \propto \eta^{\gamma}$, with $\gamma < 0.15$. We also estimated the reconnection rate as the product between the input velocity and the transverse magnetic field and arrived at the same conclusion.

The distribution of positive electric current density shown in Figure 4*b* displays fragments that were completely absent a short time ago. This development of fine structure was already envisaged by LaRosa & Moore (1993). In their paper, a picture of the development of turbulence during

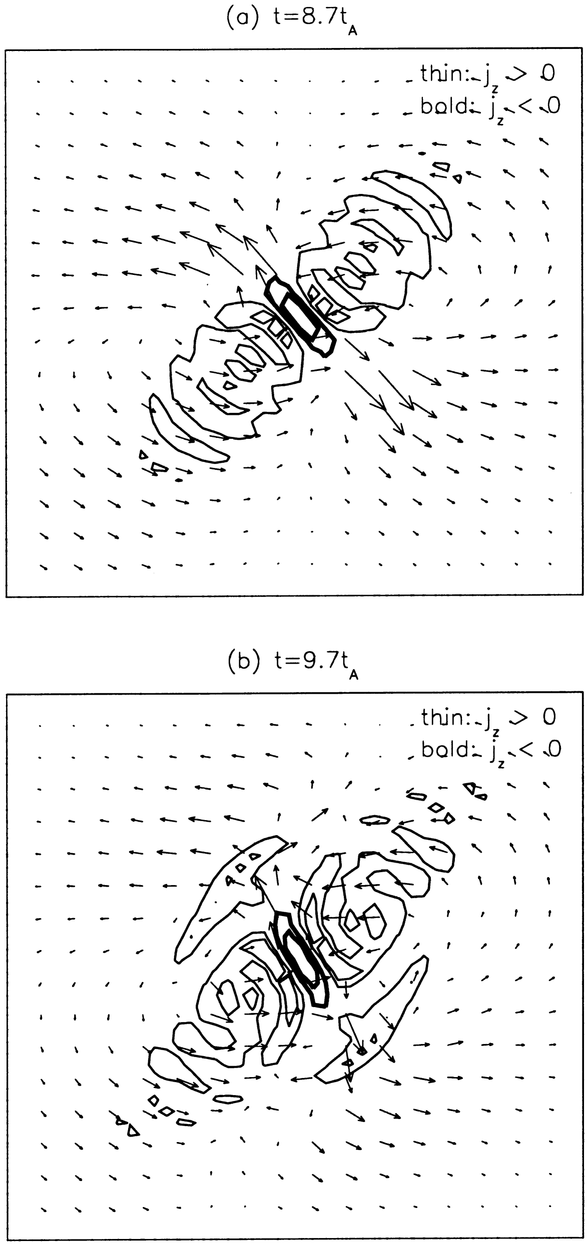

FIG. 4.—Velocity field and vertical component of electric current density j at the half-length of the loop ($z = 0.5$) at (a) $t = 8.7t_A$ and (b) $t = 9.7t_A$. Bold contours enclose the negative current layer. The Alfvénic jets shown in panel a have lost spatial coherence in panel b, and current density looks more fragmented.

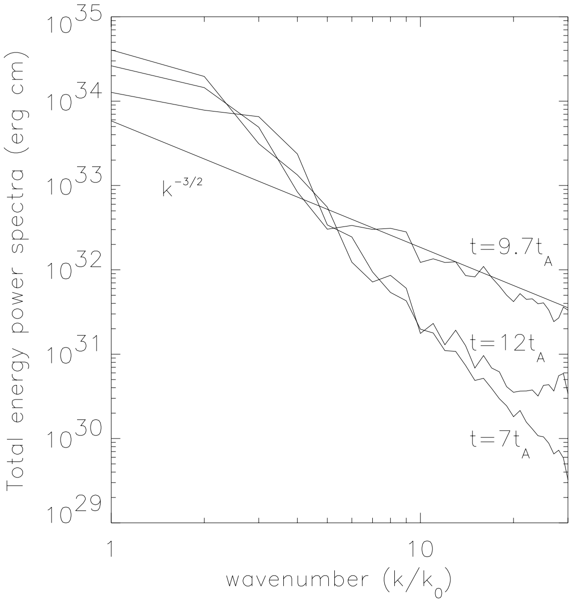

FIG. 5.—Energy power spectra at different times ($t = 7t_A$, $9.7t_A$, $12t_A$). The spectrum is flatter during reconnection ($t = 9.7t_A$). The 3/2 slope corresponds to the Kraichnan regime of fully developed MHD turbulence.

externally driven reconnection in flares is presented (see also Matthaeus & Lamkin 1986 for numerical simulations of turbulent magnetic reconnection). As shown below, our simulations support this general scenario, at least for the rather simple geometry implied by an RMHD model, which might be associated with microflares taking place inside isolated coronal loops. However, the development of fine structure alone does not necessarily imply the presence of a turbulent regime. A more precise characterization of the fine scales arising from the reconnection process can be attained by considering the energy power spectra, as shown in Figure 5. The general properties of MHD turbulence are relatively well known, at least for the special case of a homogeneous, stationary, and isotropic regime (see, for instance, Biskamp 1993 for a recent review). One of the important features of such systems is the development of an energy cascade, which is a net energy transfer from the (usually) large scales where external forces operate down to very small scales where resistive or viscous dissipation are dominant. This cascade process is consistent with the so-called Kraichnan spectrum, i.e., $E(k) \propto k^{-3/2}$, in the wavenumber range between the externally driven scales and the dissipative region. The development of MHD turbulence in nonstationary and inhomogeneous situations has also been studied, for instance, in connection with magnetic reconnection processes. The development of Kraichnan energy spectra during magnetic reconnection has been observed both in two-dimensional (Matthaeus & Lamkin 1986) and RMHD (Hendrix & van Hoven 1996) numerical simulations. Both studies report the development of a Kraichnan spectrum in conjunction with the achievement of a maximum in the energy dissipation rate. In the present paper, a power-law spectrum with an approximately $-3/2$ slope is present at $t \approx 9t_A$, which is indicative of a fully developed turbulent state. Spectra with much steeper negative slopes are present before and after the reconnection process. It seems natural that the coalescence of the flux tubes triggers a strongly nonlinear process involving all spatial scales, as indicated by a broadband power spectrum.

It is important to note that the existence of this turbulent transient might well pass unnoticed, at least if one concentrates on the global or macroscopic aspects of the evolution. The large-scale features of this reconnection process display a rather organized magnetic X-type topology with the ensuing Alfvénic jets at both sides of the current layer, as shown in Figure 4. However, the intense growth of current density in a highly localized region of space around the X-point indicates the systematic excitation of small-scale Fourier modes with a high degree of phase coherence. This rather abrupt transfer of current-carrying excitations from

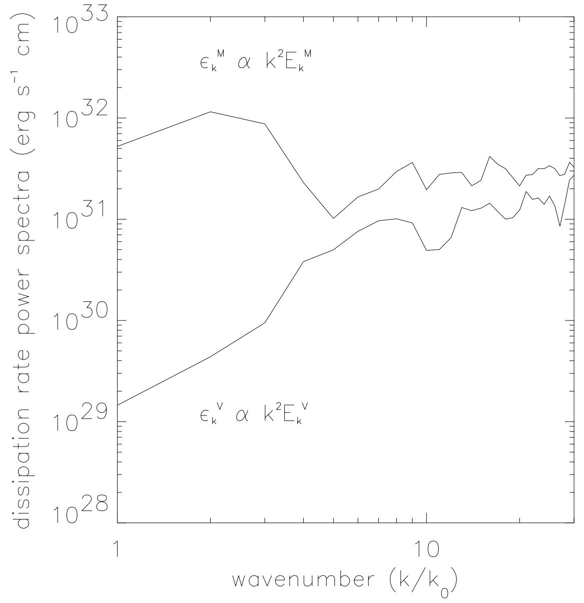

FIG. 6.—Kinetic and magnetic energy dissipation power spectra at $t = 9.7t_A$. Large-scale dissipation is essentially magnetic, while small-scale dissipation grows like $k^{1/2}$ and has comparable contribution from velocity and magnetic fields.

large scales to small scales can be naturally explained as being produced by the direct energy cascade of the turbulent transient. The energy cascade itself is essential for understanding the intense energy dissipation that takes place during this reconnection event, as discussed below.

Figure 6 shows magnetic and kinetic energy dissipation power spectra at time $t = 9.7t_A$ (total dissipation is proportional to the area below these curves). As expected for $k^{-3/2}$ energy spectra, $\epsilon_k^{V,M} \propto k^2 E_k^{V,M} \sim k^{1/2}$, that is, smaller scales dissipate more energy than larger scales. Figure 2 also shows that during reconnection kinetic and magnetic dissipation are comparable, even though the total magnetic energy is 2 orders of magnitude larger than the total kinetic energy. By looking at Figure 6, the reason is very clear: small-scale fluctuations tend to equipartition as assumed by Kraichnan (1965). However, most of the contribution to the total energy comes from large scales ($k \sim 1$), where the magnetic field is fairly dominant.

Note that before and after the reconnection event energy power spectra fall steeper than k^{-2} (Fig. 5). Therefore, the dissipation rate is a decreasing function of k, indicating that most of the dissipation comes from macroscopic spatial structures. As a result, except for the reconnection process itself, the evolution of the system is largely ideal. In summary, the peak in the dissipation rate shown in Figure 2 is intimately related to an efficient transfer of energy to small scales, which is a typical feature of turbulent regimes.

5. QSLS AND ENERGY DISSIPATION

5.1. *Definition*

QSLs are the generalization of separatrices to any kind of magnetic configuration. The QSL concept is not linked to a local criterion, as could be the presence of magnetic nulls or field lines tangential to a boundary, which are classically used to locate separatrices. QSLs are defined by the global mapping of the magnetic field. They are regions where field lines initially close to one another at a certain location separate widely when going far from that location. In the solar context, line tying to the photosphere is fundamental for the evolution of the coronal field, and it is this linkage that should be taken into account when computing QSLs. Let us integrate in both directions a field line starting at point $P(x, y, z)$ in the corona until the photospheric boundary is reached, and let $P'(x', y', z')$ and $P''(x'', y'', z'')$ be the photospheric footpoints of this line. The two endpoints define a vector $\boldsymbol{D}(x, y, z) = \{x'' - x', y'' - y', z'' - z'\}$ which describes the mapping. A rapid change in field line linkage means that for a slight shift of point $P(x, y, z)$, $\boldsymbol{D}(x, y, z)$ varies by a large amount. In our coronal loop model, the photosphere is represented by two parallel planes where $(z'' - z')$ is a constant and the large aspect ratio of the loops implies that the derivatives in z have a negligible contribution; therefore, the displacement gradient tensor M is defined by

$$M = \begin{bmatrix} \partial(x'' - x')/\partial x & \partial(x'' - x')/\partial y \\ \partial(y'' - y')/\partial x & \partial(y'' - y')/\partial y \end{bmatrix} . \tag{12}$$

As discussed by Priest & Démoulin (1995) and Démoulin et al. (1996a), the best measure of the presence of QSLs is given by the norm N of the tensor M:

$$N(x, y) = \left\{\left[\frac{\partial(x'' - x')}{\partial x}\right]^2 + \left[\frac{\partial(x'' - x')}{\partial y}\right]^2 + \left[\frac{\partial(y'' - y')}{\partial x}\right]^2 + \left[\frac{\partial(y'' - y')}{\partial y}\right]^2\right\}^{1/2} . \tag{13}$$

In general, the displacements of the photospheric footpoints of very close field lines are of the same order of magnitude, meaning that $N \approx 1$, except in localized regions where N takes larger values. The field lines in these regions are the ones characterizing QSLs, and therefore we trace many of these lines to locate QSLs in the corona. Hereafter we use the term quasi-separatrix layers method (QSLM) to refer to the numerical code used to compute the location of QSLs (Démoulin et al. 1996a).

5.2. *QSLs in the Coronal Loop Model*

We apply the QSLM to the result of our RMHD numerical simulations for the case of $S = 500$. Figures 7*a*–7*d* show the evolution of QSLs and of j at the loop half-length ($z = 0.5$) for different times. In these figures QSLs are represented by isocontours of N. Two facts become evident from Figures 7*a*–7*d*. On one side, we find a remarkable coincidence between the locations of QSLs and of the current layer developed during the coalescence of the two twisted flux tubes. On the other, we observe that there exists a close relationship between the distribution of j along the layer and the degree of distortion of the field line mapping. As the current layer grows in breadth and its electric current density increases, QSLs extend in size overlaying the layer and the value of N increases by orders of magnitude, in agreement with the result of Longcope & Strauss (1994b). We use the term " breadth " for the longest dimension of the current sheet in the (x, y)-plane, while we use " thickness " for the shortest dimension in this plane.

Figure 8 shows the isocontours of j (Fig. 8*a*) and the location of QSLs (Fig. 8*b*), computed at the time of

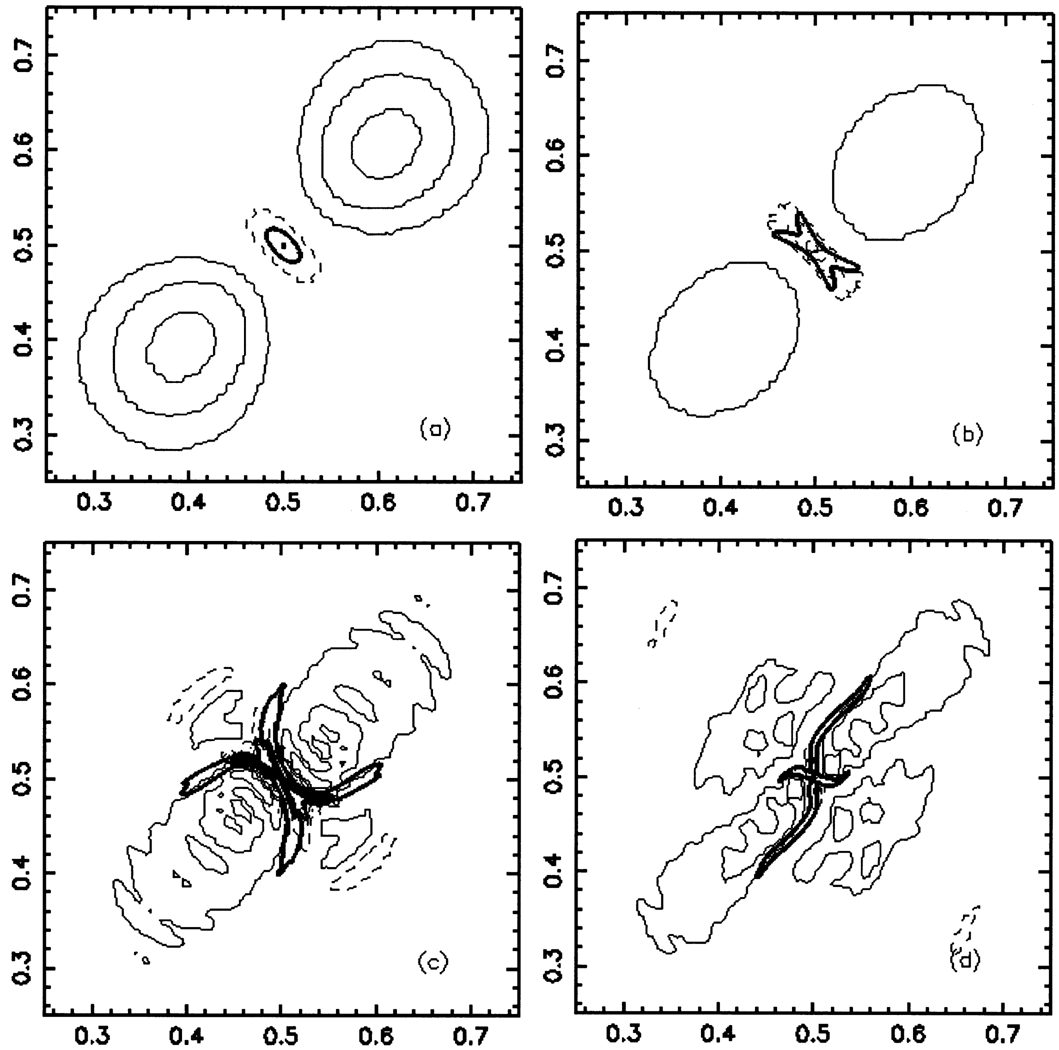

FIG. 7.—Temporal evolution of the QSL located at the half-height of the loop. (*a*) A cut of the loop at $z = 0.5$ at $t = 4t_A$. Thick lines correspond to an isocontour of $N = 5$, while thin lines show isocontours of $j = \pm 0.4, \pm 0.8, \pm 1.6$ mÅ m^{-2} (*solid line*: positive current; *dashed line*: negative current). (*b*) Same as *a*, but at $t = 7t_A$. In this case, as in *c* and *d*, we show isocontours of $N = 50$, 100 and of $j = \pm 1.2, \pm 2.4, \pm 3.6$ mÅ m^{-2}. (*c*) Same as *b*, but at $t = 9t_A$. (*d*) Same as *b*, but at $t = 11t_A$.

maximum energy dissipation ($t \approx 9t_A$) in three different planes ($z = 0$, $z = 0.5$, and $z = 1$). When comparing these two figures, the close correspondence between QSLs and the current layer at all heights becomes apparent. On the other hand, Figure 9*a* illustrates the change of connectivity between field lines located at both sides of the QSL at $z = 0$, showing the complex field line linkage existing in these regions. For clarity, we are only representing half of the surface of field lines starting from the contour of $N = 10$ (close to the border of the QSL).

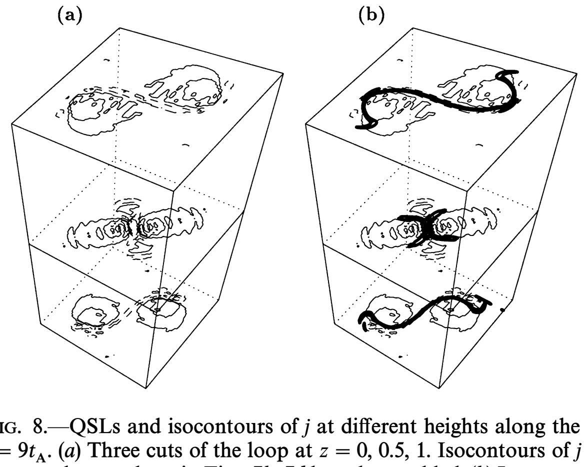

FIG. 8.—QSLs and isocontours of *j* at different heights along the loop at $t = 9t_A$. (*a*) Three cuts of the loop at $z = 0$, 0.5, 1. Isocontours of *j* with the same values as those in Figs. 7*b*–7*d* have been added. (*b*) Isocontours of *N* as in Figs. 7*b*–7*d* are shown here.

Démoulin & Priest (1997) computed QSLs in the case of a static configuration formed by the superposition of a uniform magnetic field along *z* with the field created by two vertical current kernels. Although in the present paper the fields are evolved following a fully nonlinear and dissipative simulation, the overall topology is expected to be quite similar to the one of the much simpler model studied by Démoulin & Priest (1997), since in both cases the source of magnetic field is dominated by equally signed electric current kernels. We have computed the location of QSLs for the solution of the linearized RMHD equations given by equation (11), evaluated at $t = 9t_A$, at different heights along the loop. Figure 9*b* displays the change of connectivity for field lines at both sides of the QSL for the linear solution. One of the important results of this paper is the remarkable correspondence between Figures 9*a* and 9*b* (also compare our Fig. 9*b* with Fig. 1 in Démoulin & Priest

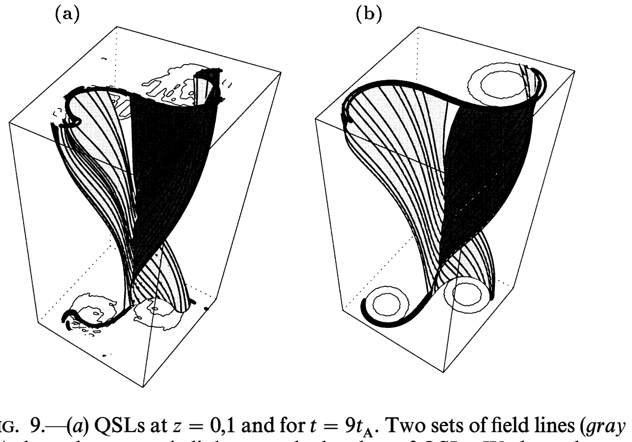

FIG. 9.—(*a*) QSLs at $z = 0,1$ and for $t = 9t_A$. Two sets of field lines (*gray areas*) show the magnetic linkage at the borders of QSLs. We have drawn these sets integrating field lines with footpoints at both sides of the right half of the QSL at $z = 0$. Two equivalent sets (not shown) could be drawn starting at the left half of the same QSL. (*b*) Same as *a*, but for the linearized solution of the RMHD equations.

1997). This indicates that the location and shape of QSLs are given by the global magnetic field configuration. Although the full simulation (when compared with the linear solution) contains nonlinear interactions and dissipation, these effects seem rather irrelevant for determining the location of the QSLs (i.e., the location of the current layer). On the other hand, as discussed in the previous section, nonlinearities are essential in other important aspects of this problem, like the development of turbulence or the ensuing increase in energy dissipation.

QSLs are very flat volumes, the thicknesses of which have been shown to be associated to the energy release rate in observed magnetic configurations (Mandrini et al. 1996). Infinitely thin QSLs arise whenever a magnetic null point is present in the field. In this case, QSLs are classical separatrices. Inside the QSLs shown in Figures 7, 8, and 9 the function N takes much larger values in thinner regions. We can analyze the behavior of N by integrating field lines along a segment orthogonal to the QSL at some localized

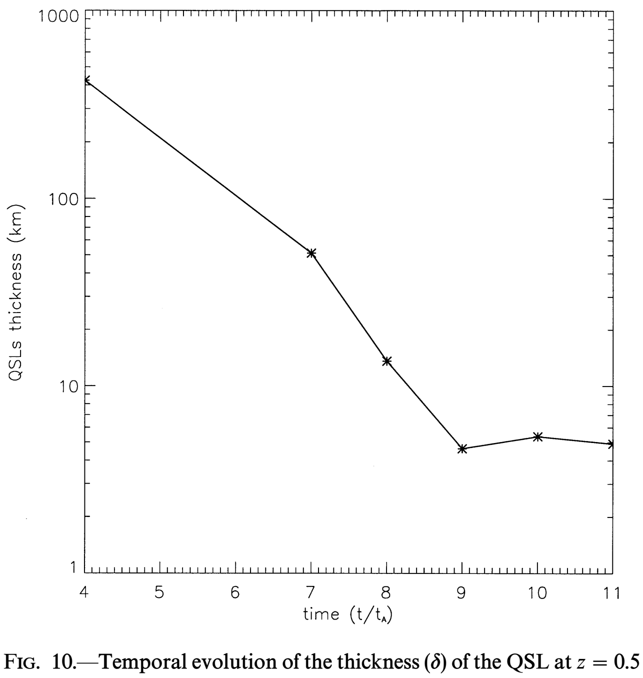

FIG. 10.—Temporal evolution of the thickness (δ) of the QSL at $z = 0.5$

point. In this way we obtain the local shape of N. The thickness δ of a QSL is defined as the width of the function N at half-height. We have computed δ at different times, as shown in Figure 10. We find that from $t = 0$ to $t \approx 9t_A$ the thickness of the QSL decreases by 2 orders of magnitude, all along the loop length. At $9t_A$ the thickness of the QSL ($\delta \approx 5$ km) is such that magnetic energy can be efficiently dissipated in that region, as shown in our numerical simulations. Furthermore, there is a direct relationship between the increase of the electric current density and the decrease of thickness of the QSL (compare, for instance, Fig. 7 with Fig. 10). After $t \approx 9t_A$, δ stays approximately constant and equal to its previous value. For both observed and theoretical configurations (Mandrini et al. 1997; Démoulin et al. 1996b, 1997) we find that δ is inversely proportional to the maximum value of N (N_{max}). The same is true in this case until $t \approx 9t_A$, which is the proportionality factor equal to 0.3. Afterward, this factor decreases by approximately 1 order of magnitude at $t = 11t_A$. We believe that this is linked to the fact that the topological structure built up by the evolution of the system breaks down and the magnetic links change drastically after magnetic reconnection has occurred.

6. CONCLUSIONS

In the present paper we study the dynamics of a typical case of an externally driven magnetic configuration leading to the coalescence of two flux tubes. The important results of this study are summarized as follows:

1. We find an excellent match between the locations of QSLs and the (negative) current layer, as shown, for instance, by Figure 8. Furthermore, there exists a close relationship between the spatial distribution of j along the layer and the degree of distortion of the field line mapping. That is, as the current layer grows in breadth and its electric current density increases, QSLs extend in size, overlaying it, and the value of N increases by orders of magnitude. This results confirms that QSLs are reliable in identifying prospective sites for magnetic reconnection.

2. The information about the sites and shapes of current layers given by the QSLs is already present in the linear solution shown in equation (11), as arises from a comparison between Figure 9*a* and Figure 9*b*. The linear solution corresponds to the magnetic configuration generated by two parallel current kernels superposed to a vertical and uniform magnetic field, as discussed by Démoulin & Priest (1997). This capacity of the linear solution to appropriately predict the location and shape of QSLs clearly indicates that the characteristics of QSLs are determined by the global magnetic field configuration, as has been discussed in previous papers (see, for instance, Mandrini et al. 1997 and references therein). Although nonlinearities play a crucial role in other aspects of the dynamics, notably the transient enhancement of energy dissipation, they seem rather unimportant in determining the sites of impulsive energy release. Note that the close correspondence between QSLs from linear versus nonlinear simulations is obtained for the particular case of an initial magnetic field driven by a stationary velocity field with a stagnation point at the origin. Therefore, we should be cautious when trying to extend this correspondence to more general configurations.

3. Our results are consistent with the picture of turbulent reconnection. The interaction between flux tubes triggers a

strongly nonlinear process involving all spatial scales, as indicated by Kraichnan's power spectrum shown in Figure 5. During this turbulent transient, energy is transferred in a cascade process to smaller scales where it is efficiently dissipated. The enhanced dissipation observed during the reconnection process is not only restricted to the current layer predicted by the QSLM, but also overshoots to its surroundings, where very fine structure is developed. It is important to stress that for the global or large-scale aspects of the evolution, the existence of this turbulent transient might pass unnoticed.

4. The overall characteristics of the turbulent reconnection process discussed in this paper are quite consistent with the scenario put forward by LaRosa & Moore (1993) to describe the impulsive phase of solar flares. However, because of the geometrical assumptions implied by the RMHD equations, the present analysis should be associated with microflares rather than flares. Microflares are transient brightenings observed in soft X-rays, presumably taking place inside single loops (see, for instance, Shimizu 1995 for an extended observational analysis of these events). According to the present study, in order for a microflare of 10^{26}–10^{27} ergs to occur inside a loop, a spatially coherent photospheric velocity field should be applied to the loop footpoints during times long enough to trigger the coalescence process.

We acknowledge financial support from the University of Buenos Aires (grant TX065/98) and CONICET (grants PEI 105/98 and PEI 104/98). Economic support from ANPCYT (Argentina) and ECOS (France) through their Argentina-France cooperative science program (A97U01) is also acknowledged.

REFERENCES

Alissandrakis, C. E. 1981, A&A, 100, 197
Aulanier, G., Démoulin, P., van Driel-Gesztelyi, L., Mein, P., & DeForest, C. 1998, A&A, 335, 309
Biskamp, D. 1993, Nonlinear Magnetohydrodynamics (Cambridge: Cambridge Univ. Press)
Canuto, C., Hussaini, M. Y., Quarteroni, A., & Zang, T. A. 1988, Spectral Methods in Fluid Dynamics (New York: Springer)
DeLuca, E., & Craig, I. 1992, ApJ, 390, 679
Démoulin, P., Bagalá, L. G., Mandrini, C. H., Hénoux, J. C., & Rovira, M. G. 1997, A&A, 325, 305
Démoulin, P., Hénoux, J. C., Priest, E. R., & Mandrini, C. H. 1996a, A&A, 308, 643
Démoulin, P., & Priest, E. R. 1997, Sol. Phys., 175, 123
Démoulin, P., Priest, E. R., & Lonie, D. P. 1996b, J. Geophys. Res., 101, 7631
Dmitruk, P., Gómez, D. O., & DeLuca, E. E. 1998, ApJ, 505, 974
Galsgaard, K., & Nordlund, A. 1996, J. Geophys. Res., 101, 13445
Hendrix, D. L., & van Hoven, G. 1996, ApJ, 467, 887
Jardine, M. 1991, in Mechanisms of Chromospheric and Coronal Heating, ed. P. Ulmschneider, E. R. Priest, & R. Rosner (Berlin: Springer), 588
Kraichnan, R. H. 1965, Phys. Fluids, 8, 138
Lau, Y. T., & Finn, J. M. 1991, ApJ, 366, 577
LaRosa, T. N., & Moore, R. L. 1993, ApJ, 418, 912
Longcope, D. W., & Strauss, H. R. 1994a, ApJ, 426, 742
———. 1994b, ApJ, 437, 851
Mandrini, C. H., Démoulin, P., Bagalá, L. G., van Driel-Gesztelyi, L., Hénoux, J. C., Schmieder, B., & Rovira, M. G. 1997, Sol. Phys., 174, 229
Mandrini, C. H., Démoulin, P., van Driel-Gesztelyi, L., Schmieder, B., Cauzzi, G., & Hofmann, A. 1996, Sol. Phys., 168, 115
Matthaeus, W. H., & Lamkin, S. L. 1986, Phys. Fluids, 29, 2513
Mikic, Z., Schnack, D., & van Hoven, G. 1989, ApJ, 338, 1148
Priest, E. R. 1997, Phys. Plasmas, 4 (5), 1945
Priest, E. R., & Démoulin, P. 1995, J. Geophys. Res., 100, 23443
Shimizu, T. 1995, PASJ, 47, 251
Strauss, H. 1976, Phys. Fluids 19, 134
van Ballegooijen, A. 1986, ApJ, 311, 1001